Nano-sized ZIF-8 anchored polyelectrolyte-decorated silica for Nitrogen-Rich Hollow Carbon Shell Frameworks toward alkaline and neutral supercapacitors

Zhiwei Li [a], Hongyu Mi [a, *], Lang Liu [a], Zhengyu Bai [b], Jinping Zhang [a], Qing Zhang [b], Jieshan Qiu [c, **]

[a] Key Laboratory of Energy Materials Chemistry (Xinjiang University), Ministry of Education, Institute of Applied Chemistry, School of Chemistry and Chemical Engineering, Xinjiang University, Urumqi 830046, China
[b] School of Chemistry and Chemical Engineering, Key Laboratory of Green Chemical Media and Reactions, Ministry of Education, Henan Normal University, Xinxiang 453007, China
[c] School of Chemical Engineering and Technology, Xi'an Jiaotong University, Xi'an 710049, China

A B S T R A C T

Core-shell hybrid precursors (ZIF-8/*PP*-SiO$_2$) engineered by zeoliticimidazolate framework (ZIF-8) depositing on the polyelectrolyte-decorated silica (*PP*-SiO$_2$) are successfully transformed into unusual N-rich hollow carbon shell frameworks (NHCSFs) with adjustable physicochemical properties by the layer-by-layer assembly, interface engineering and subsequent carbonization, which is the first example that systematically elucidates the formation and structure-property correlation of unique three-dimensional (3D) carbon frameworks. The optimal NHCSF-3 displays superior performance with high capacitance approaching 253.6 F g^{-1} at 1 A g^{-1}, excellent rate capability delivering 79% capacitance retention after a 50-fold increase of the rate, and long lifetime (92.1% retention for 20000 cycles). The studies on alkaline and neutral NHCSF-3//NHCSF-3 supercapacitors demonstrate that the latter with high voltage up to 1.6 V using a Na$_2$SO$_4$ electrolyte can deliver high energy density of 13.3 Wh kg^{-1}. The distinctly enhanced performance illustrates that, except for the factors such as morphology, surface area, pore volume, and N-doping level, hierarchical porosity also significantly boosts electrochemical properties of the materials because of providing efficient charge/mass transport. Overall, this research provides an efficient platform for precisely modulating the structure of MOF-based carbons to develop multifunctional hollow architectures for satisfying enormous demands in upcoming energy devices.

© 2018 Elsevier Ltd. All rights reserved.

1. Introduction

With the ever-growing and imperative demands in efficient and renewable energy due to global energy crisis and environmental deterioration in recent decades, eco-friendly and efficient electrochemical capacitors (ECs) or supercapacitors (SCs) as upcoming advanced devices, which are mainly sorted into electric double-layer capacitors (EDLCs) and pseudocapacitors, have been rapidly developed. SCs integrate the merits of conventional dielectric capacitors and batteries, showing distinct superiority in power delivery, charge/discharge capability, recyclability, and safety [1]. For these reasons

SCs are widely employed in consumer electronics, internal back-up power, industrial power management, and electric vehicles [2–5].

Hollow porous carbons are acknowledged as interesting and promising carbon forms for energy storage and thus inspire a particular attention from researchers. On the one hand, they share common intrinsic properties of carbon materials, including outstanding physicochemical properties (i.e., natural abundance, non-toxicity, high conductive and mechanical properties, long lifetime, and high safety) and high utilization (commercial carbon-based SCs of over 80% in the market) [6–9]. On the other hand, they exceptionally exhibit some unique characteristics like special shape, low density, controllable cavity volume, short ion/electron transport length, and high contact area for the electrolyte [10–13]. Hollow architectures have been typically prepared by the template-assisted method using different precursors [13–22]. Recent

* Corresponding author.
** Corresponding author.
  E-mail addresses: mmihongyu@163.com (H. Mi), jasonqiu@xjtu.edu.cn (J. Qiu).

achievements on the template approach have proven that its conspicuous advantage is the straightforward and precise control over the morphology and size of the materials [21,23]. Subsequent focus has been paid on high-activity hollow carbons doped by heteroatoms situated in carbon frameworks [24–28], since these heteroatoms can contribute extra pseudocapacitance [29,30]. Lou and co-workers well integrated ZIF-8 into electrospun polyacrylonitrile (PAN) to construct hollow particle-based N-doped carbon nanofibers [12]. This electrode displayed remarkable high capacitance of 307.2 F g^{-1} at 1.0 A g^{-1}, high energy/power density up to 10.96 Wh kg^{-1} and 25000 W kg^{-1}, and long-term stability with a decay of 1.8% loss up to 10000 cycles. As reported by Li and Wang et al. [27], monodispersed N-doped hollow carbon nanospheres prepared by a modified "silica-assisted" procedure, reached high capacitance of 240 F g^{-1} at 1 A g^{-1} and high capacitance retention of 97.0% after 5000 cycles, significantly better than the results of non-doping hollow carbons. N-doped hollow carbon capsules were also synthesized using polyacrylonitrile precursors by the "dissolution-capture" method, which manifested excellent electrochemical results attributable to the N-doped hollow structures with favourable textural properties [28]. These reports have confirmed the strong dependence of the performance on structure, and thus structural exploration to create novel energy storage materials would be a long-term and vital task in energy fields.

Metal organic frameworks (MOFs), well known for diverse inorganic-organic hybrid crystals, tailorable components, highly accessible surface area and nano-sized cavities, are typically built from the supramolecular assembly of metal ions/metal clusters with organic linkers. In MOFs, organic component acts as carbon source/pore maker while inorganic component for yielding more pores [31]. Thus, MOFs hold great promise for constructing advanced carbons with many structural advantages (large specific area, high porosity, and tailorable structure) for clean energy systems [22,32–42]. Of versatile MOFs, ZIF-8 (Zn [MeIM]$_2$ = ZnC$_8$H$_{10}$N$_4$, MeIM = 2-methylimidazolate) is the most widely studied due to facile synthesis on a scale. Yamauchi and Hu et al. employed monocrystalline ZIF-8 nanobubbles to synthesize hollow carbon nanobubbles with fast Na$^+$/K$^+$ ion intercalation performance [37]. Su and Wang et al. reported 3D hybrid-porous carbon from ZIF-8 precursor, which exhibited a specific capacitance as high as 332 F g^{-1} at 0.5 A g^{-1}, and outstanding stability showing no capacitance decaying up to 10000 cycles [40]. Inspired by these studies, herein, the first N-rich hollow carbon shell frameworks (NHCSFs) composed of hollow shells and two-dimensional (2D) nanoflakes are simply but uniquely synthesized by a strategy of combining layer-by-layer assembly with template method, where the in-situ growth of MOF and interface engineering are used. This assembly method can produce engineered carbon materials with unique well-developed structure, i.e. Nitrogen-Rich Hollow Carbon Shell Frameworks, which is different from the traditional hollow carbon spheres and capsules that are separated to each other. The literature survey has indicated that this kind of structure is rarely reported in literature. This research also provides in-depth insight into the formation and structure-property correlation of the concerned carbon with hierarchical porous frameworks. Based on the electrochemical evaluation in alkaline and neutral SCs, carbon shell frameworks (NHCSF-3) fabricated under the optimized conditions can deliver excellent performance, exhibiting the significant promise in energy storage fields.

2. Experimental

2.1. Chemical reagents

All reagents and chemicals are commercially obtained. Silica powder (SiO$_2$, 200–300 nm; purity: > 99.8%), poly(-diallyldimethylammonium chloride) solution (PDDA, M$_w$ ≈ 200000–350000, 20 wt%), and poly(styrene sulfonic acid sodium salt) solution (PSS, 30 wt%) were purchased from Aladdin Chemical Co., Ltd. (Shanghai, China). 2-methylimidazole was obtained from Beijing J&K Scientific Co. Ltd (Beijing, China). Prior to use, both PDDA and PSS solutions were adjusted to 1 wt%, respectively. Others, such as zinc nitrate, urea, and methanol, were directly used without further purification.

2.2. Preparation of polyelectrolyte-decorated SiO$_2$ (PP-SiO$_2$)

A certain amount of SiO$_2$ (1, 2, 3, and 4 g) was added in 80 mL of 1 wt% PDDA solution and stirred for 1 h followed by five centrifugation/washing cycles, producing PDDA-decorated SiO$_2$ (P-SiO$_2$). Similarly, P-SiO$_2$ was treated by 1 wt% PSS solution. As a result, four PSS/PDDA-modified SiO$_2$ products were obtained, which were designated as PP-SiO$_2$-1, PP-SiO$_2$-2, PP-SiO$_2$-3, and PP-SiO$_2$-4 corresponding to the use of 1, 2, 3, and 4 g of SiO$_2$.

2.3. Preparation of N-rich hollow carbon shell frameworks (NHCSF-3)

In a typical fabrication, 1.5 g of zinc nitrate was dissolved in 150 mL of PP-SiO$_2$-3 (3 g) dispersed methanol followed by stirring for 2 h. Then, a 2-methylimidazole solution (2.0 g in 150 mL of methanol) was slowly dripped into the above solution. After stirring for 12 h and aging for another 12 h, ZIF-8/PP-SiO$_2$-3 solid was collected by centrifugation, washing with methanol for three times, and drying at 80 °C. This method of making core-shell structure by depositing ZIF-8 on modified silica was similar to that reported previously [43]. Next, these white powders were thermally annealed for 2 h at 800 °C under N$_2$ flow, with a ramp rate of 2 °C min^{-1}. The treated intermediates were orderly immersed in 1 M HCl and 5% HF solutions for several days, and then collected and thoroughly rinsed with distilled water for the removal of Zn species and SiO$_2$, yielding NHCSF-3.

Various carbon samples obtained using different PP-SiO$_2$ were denoted as NHCSF-1, NHCSF-2, and NHCSF-4, respectively. NHCSF-0 from ZIF-8 was synthesized without SiO$_2$ addition. In addition, the mediate ZIF-8/SiO$_2$-3 using SiO$_2$-3 (3 g SiO$_2$) instead of PP-SiO$_2$-3 was yielded according to the above described route for comparison. In order to clarify the structure of NHCSF-3, graphitic carbon nitride (g-C$_3$N$_4$) was prepared by a method reported [44]. Typically, urea was thermally treated in air for 2 h at 550 °C, with a ramp rate of 5 °C min^{-1}, producing g-C$_3$N$_4$.

2.4. Physical and chemical characterizations

The morphological observation was conducted on a SU4800 scanning electron microscope (SEM, Japan), Hitachi-600 and JEM-2100F transmission electron microscopes (TEM, Japan). Spectral properties of the products were examined by Fourier transform infrared (FTIR) spectroscopy on a Brüker VERTEX70 spectrometer (Germany). Crystal structure and purity of the products were observed by X-ray diffraction (XRD) using a Brüker D8 Advance (Germany), with a Cu Ka target (λ = 1.54056 Å). X-ray photoelectron spectroscopy (XPS) was collected on a Thermo Fisher Scientific ESCALAB 250Xi system (USA) for studying surface chemical state. The N content of the optimized sample was measured by a CHN element analyzer (Germany, Vario EL cube). Textural properties were examined on a 3H-2000PM1/2 N$_2$ sorption instrument (China), where specific surface area and pore size distribution were calculated by Brunauer-Emmett-Teller (BET) method and the Barrett-Joyner-Halenda (BJH) model, respectively. Thermogravimetric (TG)

curve was recorded from room temperature to ~1000 °C under air flow using a SDTQ600 Thermoanalyzer (USA), with a heating rate of 5 °C min^{-1}.

2.5. Electrochemical measurements

The electrochemical tests were conducted on a CHI660 electrochemical working station (China) and a CT2001A cycling test system (China). The used three-electrode cell consisted of a working electrode (NHCSFs), a platinum counter electrode, and a Hg/HgO reference electrode. To prepare the working electrode, 80 wt% porous carbons obtained, 10 wt% acetylene black, and 10 wt% polytetrafluoroethylene were ultrasonically mixed in a solution of distilled water and ethanol, and then dried. The obtained sticky mixture was roll-pressed into thin sheet, cut into small pieces, and finally pressed on the nickel foam current collector. The loading mass of active material was approximately 2.0 mg cm^{-2}. The two-electrode symmetrical SC based on NHCSF-3 electrodes using Whatman filter paper as the separator was investigated in 6 M KOH and 1 M Na$_2$SO$_4$ aqueous electrolytes, respectively. The specific capacitance (C_m, F g^{-1}) in three-electrode system was calculated through eqn. (1) [26]:

$$C_m = I\Delta t/m\Delta V \tag{1}$$

where I (A) represents the discharge current, and Δt (s), m (g), and ΔV (V) are the discharge time, the mass of active material, and the discharge voltage excluding IR drop (V), respectively.

In a symmetric two-electrode cell, the specific capacitance (C_s, F g^{-1}) of single electrode, power density (P, W kg^{-1}), and energy density (E, Wh kg^{-1}) were calculated through eqns. (2)–(4) [5,12]:

$$C_s = 2I\Delta t/m\Delta V \tag{2}$$

$$E = C_s\Delta V^2 \big/ (8 \times 3.6) \tag{3}$$

$$P = 3600E/\Delta t \tag{4}$$

where m (g) is the mass of active material in single electrode.

3. Results and discussion

3.1. Synthesis of NHCSF-3

Typical synthetic strategy for ZIF-8/PP-SiO$_2$-3 derived NHCSF-3 is schematically described in Fig. 1. For confining ZIF-8 growth on the surface of the template, polyelectrolyte-decorated SiO$_2$ colloidal spheres (PP-SiO$_2$-3) with negative charges were initially prepared by electrostatic modification of SiO$_2$ with oppositely charged PDDA and PSS. Then, PP-SiO$_2$-3 spheres were dispersed in Zn^{2+} containing methanol solution for Zn^{2+} attaching on the PP-SiO$_2$-3 surface by electrostatic induced ion adsorption. Subsequently, 2-methylimidazole was added and reacted with Zn^{2+} by simple coordination chemistry, yielding core-shell ZIF-8/PP-SiO$_2$-3 heterostructures with nanoscale ZIF-8 particles anchoring on the PP-SiO$_2$-3 surface. The heterostructures were then carbonized and etched to form hollow carbon shell frameworks (NHCSF-3) with ultrathin walls, open holes on shells, and 3D hierarchical open nanopores. We believe that the combination of ZIF-8 with PP-SiO$_2$ can tune intrinsic properties of the resultant product.
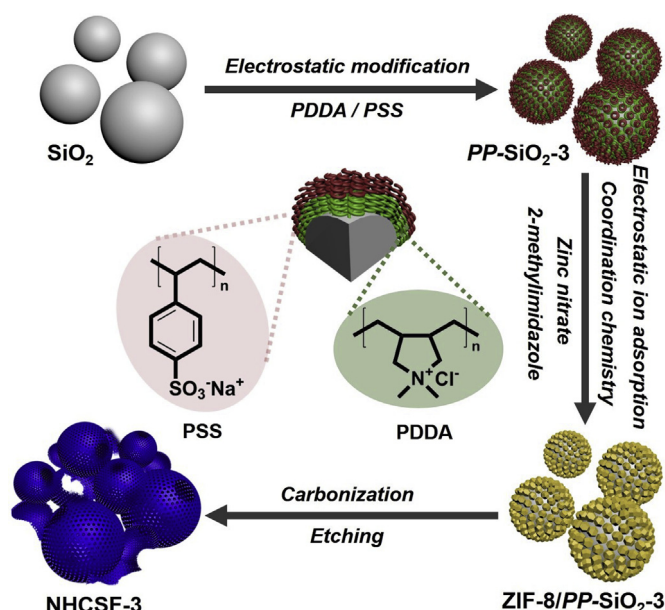

Fig. 1. Scheme depicting the fabrication of NHCSF-3 from ZIF-8/PP-SiO$_2$-3 precursor. (A colour version of this figure can be viewed online.)

3.2. Morphological evolution of NHCSF-3

The morphology formation of the NHCSF-3 can be clarified by SEM and TEM imaging, as depicted in Fig. 2. ZIF-8 particles feature as rhombic dodecahedral crystals, and the particle size is approximately 200—400 nm (Fig. 2a). The image of NHCSF-0 reveals a considerable shape resemblance to it precursor (ZIF-8) (Fig. 2b and c). This perfect morphological inherence but the decreased size is indicative of double functionalities of ZIF-8 as the in-built template and carbon source. High-resolved TEM image in Fig. 2d shows a uniform nanoporous structure of NHCSF-0, which are originated from the decomposition of organic phase and the removal of Zn^{2+} in ZIF-8 [31]. In the images of pristine SiO$_2$ (Fig. 2e) and modified SiO$_2$ (PP-SiO$_2$-3) (Fig. 2f), similar spherical shapes with a broad size distribution of around 100—400 nm infer the coating of thin polyelectrolyte layer on the SiO$_2$ surface. When the PP-SiO$_2$-3 was used as the support, the deposition of small-sized ZIF-8 nanoparticles strictly occurs on the PP-SiO$_2$-3 surface to form core-shell ZIF-8/PP-SiO$_2$-3 spheres with coarse surface (Fig. 2g). Instead, the use of untreated SiO$_2$ causes random dispersion of some ZIF-8 particles (as indicated by red circles) around the SiO$_2$ surface (Fig. 2h). Moreover, the size of these ZIF-8 particles is significantly bigger than that of ZIF-8 in ZIF-8/PP-SiO$_2$-3. It suggests that polyelectrolyte layer can assist in well deposition of ZIF-8, and control the size of ZIF crystals. In Fig. 2i, NHCSF-3 from ZIF-8/PP-SiO$_2$-3 basically remains sphere shape of the PP-SiO$_2$-3, with hollow reservoir-like structures noted from cave-like defects on carbon shells. The magnified image of NHCSF-3 (the inset in Fig. 2i) shows the connectivity of the shells (as remarked by red circles), which indicate 3D hollow shell frameworks. Mapping images of NHCSF-3 obtained from low-resolved SEM image confirm the uniform distribution of C, O and N elements, and the presence of N-doped structure (Fig. 2j). Low- and high-resolution TEM images (Fig. 2k and l) show that hollow shells with plenty of nanopores are interconnected, or connected with some porous nanoflakes that are broken shells in
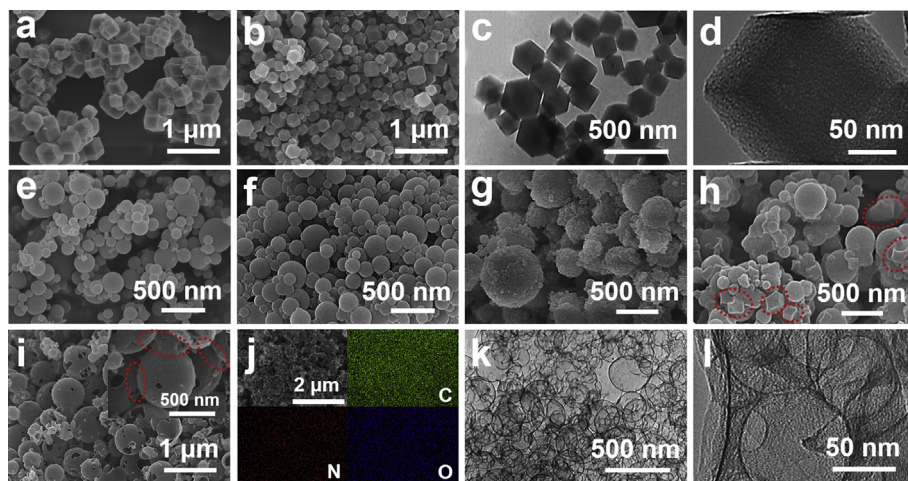
Fig. 2. SEM images of (a) ZIF-8 and (b) NHCSF-0; (c, d) low- and high-resolution TEM images of NHCSF-0; SEM images of (e) SiO$_2$, (f) PP-SiO$_2$-3, (g) ZIF-8/PP-SiO$_2$-3, (h) ZIF-8/SiO$_2$-3, and (i) NHCSF-3 (inset showing the enlarged image); (j) low-resolution SEM image of NHCSF-3 and the corresponding elemental mapping images of C, O and N, respectively; (k, l) low- and high-resolution TEM images of NHCSF-3. (A colour version of this figure can be viewed online.)

fact, constructing a hollow shell-stacked structure with 3D connectivity, which is in accord with the SEM result (the inset in Fig. 2i).

3.3. Influence of the template amount on morphology

SEM and TEM imaging were performed to provide insight into the morphology dependence on the template amount. As displayed in Fig. 3, there are clear differences in morphology for various precursors and corresponding carbons. Using 1 g PP-SiO$_2$ (PP-SiO$_2$-1), the synthesized ZIF-8/PP-SiO$_2$-1 template is hardly seen due to a large amount of ZIF-8 covering on and around PP-SiO$_2$-1 surface. With the increment of the PP-SiO$_2$ mass (PP-SiO$_2$-2, 2 g), the agglomeration of ZIF-8 nanoparticles slightly reduces (Fig. 3d). Attractively, with further increase of the template amount (PP-SiO$_2$-3, 3 g; PP-SiO$_2$-4, 4 g), well-organized core-shell structures are found in images of ZIF-8/PP-SiO$_2$-3 (Fig. 2g) and ZIF-8/PP-SiO$_2$-4

(Fig. 3g), where the distribution of ZIF-8 on the modified templates is more uniform. Moreover, the coating layer of ZIF-8 on ZIF-8/PP-SiO$_2$-4 is thinner than on ZIF-8/PP-SiO$_2$-3. It is accepted that the use of more template causes the decreased deposited amount of ZIF-8. Next, the carbons formed using different amounts of precursors are morphologically characterized by SEM and TEM, as shown in Fig. 3. All carbon architectures exhibit a continuous hollow structure but the details of the morphologies are distinguished from each other. NHCSF-1 from ZIF-8/PP-SiO$_2$-1 consists of many broken shells (namely, nanoflakes) and ZIF-8 based carbon particles (as remarked by red arrows) (Fig. 3b), which is clearly exhibited in TEM image (Fig. 3c). Some broken shells and relatively complete shells are visible in the images of NHCSF-2 (Fig. 3e and f). Regarding NHCSF-3, a well-arranged hollow framework is verified as depicted in Fig. 2i and k. However, for NHCSF-4 structural collapse happens on a majority of hollow shells, leading to the appearance of both incomplete shells and curly nanoflakes (Fig. 3h and i). The analysis
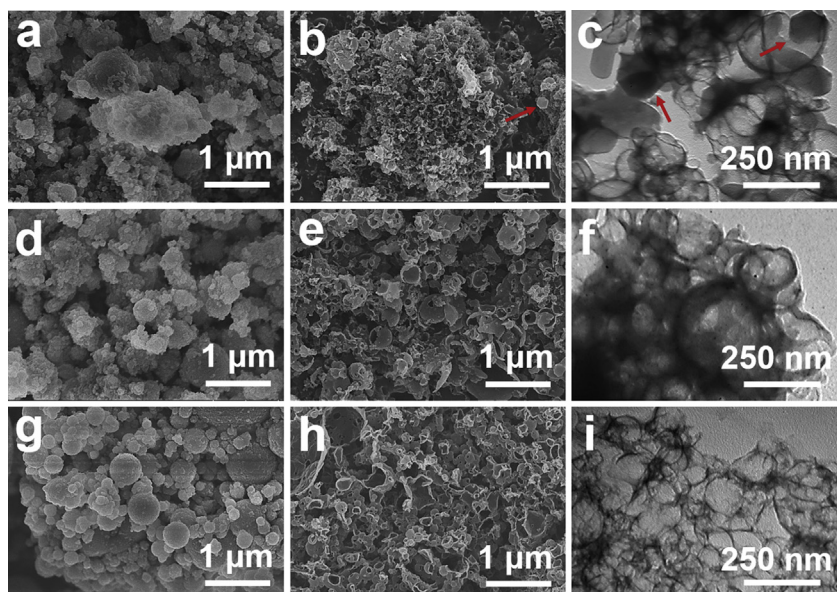
Fig. 3. SEM images of (a) ZIF-8/PP-SiO$_2$-1, (d) ZIF-8/PP-SiO$_2$-2, and (g) ZIF-8/PP-SiO$_2$-4; SEM and TEM images of (b, c) NHCSF-1, (e, f) NHCSF-2, and (h, i) NHCSF-4. (A colour version of this figure can be viewed online.)

of the morphologies identifies the success of well-adjusted morphology depending on the template amount.

3.4. Structure, pore properties, surface chemistry of various NHCSFs

XRD patterns are used to examine crystallographic features of various NHCSFs. In XRD pattern of the as-formed ZIF-8 (Fig. 4a), prominent Bragg reflections are indexed to (011), (002), (112), (022), (013), and (222) planes of rhombic dodecahedral ZIF-8 [44], respectively, which ideally coincide with those of simulated ZIF-8 crystals, suggesting the synthesis of phase-pure crystalline ZIF-8 [45–47]. Similarly, the pattern of ZIF-8/PP-SiO$_2$-3 also appears the characteristic peaks of pure ZIF-8 as a result of the generation of ZIF-8/PP-SiO$_2$-3. Broad diffraction peaks at 24.7° and 43.2° in XRD patterns (Fig. 4b) depict the amorphous nature of both NHCSF-0 and NHCSF-3 [3]. No evident reflections from Zn and other crystalline species illustrate high purity of both carbons obtained. For comparison, the pattern of g-C$_3$N$_4$ is provided in Fig. S1, which differs from those of NHCSF-0 and NHCSF-3. It shows typical (100) and (002) peaks at ~13.2° and ~27.4°, corresponding to the in-plane structural packing motif and inter-planar stacking reflection of conjugated aromatic systems, respectively, in consistent with the literature report [44]. Thus, it indicates that the structures of NHCSFs and g-C$_3$N$_4$ are different from each other.

Nitrogen sorption profiles of various NHCSFs are presented in Fig. 4c. Based on the International Union of Pure and Applied Chemistry (IUPAC) classification, the isotherm corresponding to NHCSF-0 witnesses the Type-I behavior with obvious uptake at low relative pressure ($P/P_0 < 0.01$), which prove a microporous material in NHCSF-0, in consistent with previous study [42]. However, different from NHCSF-0, other NHCSFs (NHCSF-1, NHCSF-2, NHCSF-3, and NHCSF-4) exhibit Type-IV isotherms with a prominent hysteresis loop at high relative pressure ($P/P_0 = 0.42–0.99$) (Fig. 4c), manifesting a typical mesoporous structure. Moreover, such four

samples with the aid of the template feature as hierarchical porosity because of the presence of micro- and macro-pores based on the characteristics of the isotherms at low P/P_0 value ($P/P_0 < 0.01$) and high P/P_0 value ($P/P_0 \approx 0.99$) [42]. Additionally, textural properties are provided in Table 1. All NHCSFs show relatively high BET area despite the absence of any activation. The order of the area is NHCSF-1 (585 m^2 g^{-1}) < NHCSF-4 (667 m^2 g^{-1}) < NHCSF-2 (679 m^2 g^{-1}) < NHCSF-3 (816 m^2 g^{-1}) < NHCSF-0 (847 m^2 g^{-1}). The decrease in area value of NHCSF-4 might be due to the structural stacking. Besides, the increase in total pore volume is shown with the template amount. There is an order of NHCSF-0 (0.6 cm^3 g^{-1}) < NHCSF-1 (1.30 cm^3 g^{-1}) < NHCSF-2 (1.42 cm^3 g^{-1}) < NHCSF-3 (1.85 cm^3 g^{-1}) < NHCSF-4 (3.24 cm^3 g^{-1}). It is also found that the microporous and mesoporous volumes of these samples are different. Usually, a proper ratio of micropore to mesopore might be of importance to improve the mass and electron transport. The pore size distribution (PSD) curves in Fig. 4d reveal similar mesopore sizes centering around 4.1 nm, but their micropores show a broad distribution (~0.42–1.23 nm). Generally, the capacitive performance strongly relies on pore properties of the material (i.e., BET area, pore volume, hierarchical porosity). A comprehensive analysis of these data speculates that NHCSF-3 might possess the best performance, which is demonstrated by systematic electrochemical studies. On the other hand, the presented data well highlight the superiority of the template strategy in convenient and effective development of hierarchical porosity.

TG curve of NHCSF-3 tested under air flow is depicted in Fig. 4e. A slight weight loss (4.5%) occurs below 200 °C as a result of the evaporation of adsorbed water and moisture. Between 450 and 600 °C, a remarkable mass loss appears, which is accountable to the complete decomposition of heteroatom-including carbon materials into CO$_2$, NO and trace amount of H$_2$O [48]. At ~1000 °C, the whole loss of almost 100% is the characteristic of high-purity NHCSF-3.
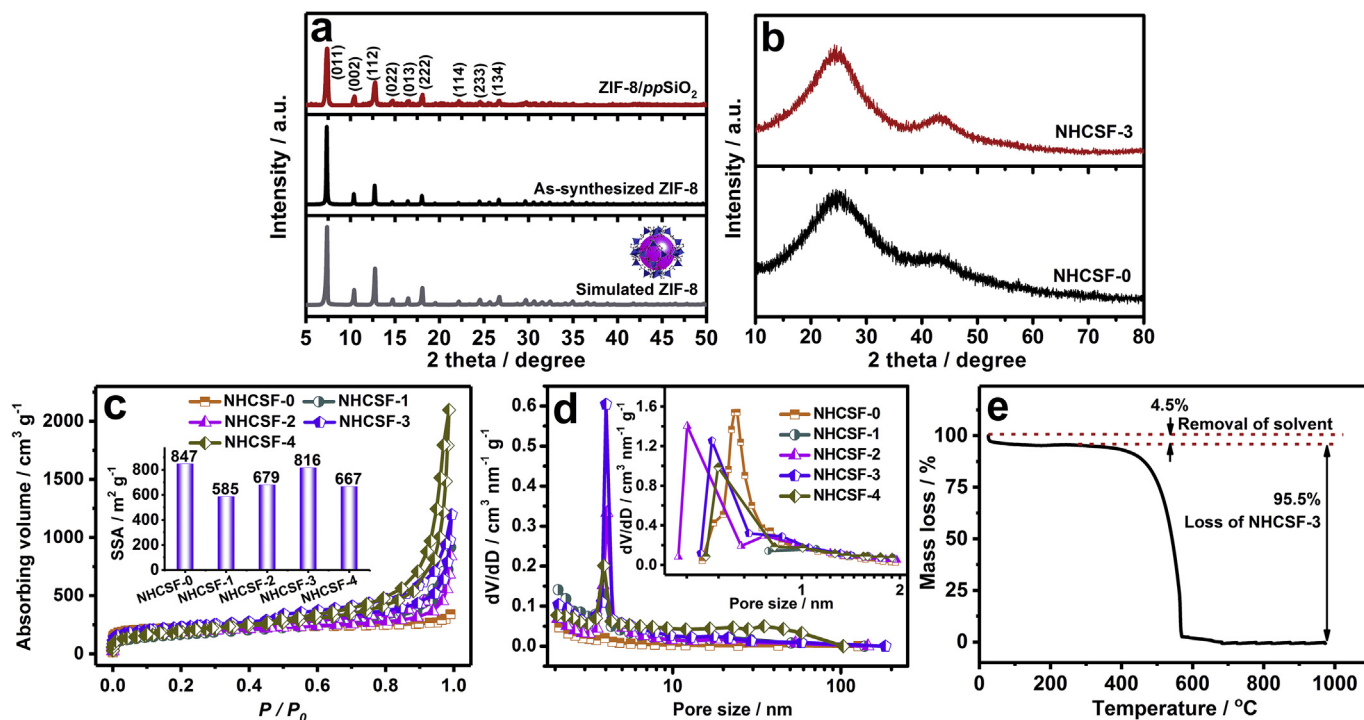
Fig. 4. (a) XRD patterns of simulated ZIF-8, as-synthesized ZIF-8, and ZIF-8/PP-SiO$_2$-3; (b) XRD patterns of NHCSF-0 and NHCSF-3; (c) N$_2$ adsorption-desorption isotherms of all NHCSFs (the inset showing BET areas); (d) mesopore size distributions of all NHCSFs (the inset showing micropore size distributions); (e) TG curve of NHCSF-3 in air flow. (A colour version of this figure can be viewed online.)

Table 1
Textural parameters of various NHCSFs.

Sample	S_{BET}[a]/m² g⁻¹	V_T[b]/cm³ g⁻¹	V_{Micro}[c]/cm³ g⁻¹	V_{Meso}[d]/cm³ g⁻¹	D_{ap}[e]/nm
NHCSF-0	847	0.52	0.33	0.19	2.49
NHCSF-1	585	1.30	0.30	1.00	9.68
NHCSF-2	679	1.42	0.28	1.14	7.64
NHCSF-3	816	1.85	0.27	1.58	9.07
NHCSF-4	667	3.24	0.25	2.99	19.46

[a] Specific surface area.
[b] Total pore volume.
[c] Micropore volume.
[d] Mesopore volume.
[e] Average pore diameter.

XPS spectra are presented for elucidating surface compositions of NHCSF-0 and NHCSF-3. XPS spectra of g-C₃N₄ are also presented in Fig. S2 for comparison. In Fig. 5a and Fig. S2a, the signals of C 1s, N 1s, and O 1s are seen at 284.4 eV, 400 eV, and 531 eV, respectively. It is noted from Table 2 that the N contents of NHCSF-0 and NHCSF-3 are as high as 20.04 and 20.29 at%. Further, the optimal sample (NHCSF-3) is verified to contain 19.47 wt% N by elemental analysis, nearly in consistent with the XPS result. These values are slightly lower than previously reports (21.2 at% N for NDCFs [49], 20.4 wt% for N-CNB8 [50]), but still much lower than that of g-C₃N₄ (55.49 at %) (Fig. S2a). High-resolution N 1s spectra of NHCSF-0 and NHCSF-3 are given in Fig. 5b. The fitted N1s spectrum shows the bonds of pyridinic N (N-6, 398.9 eV), pyrrolic N (N-5, 400.6 eV), quaternary-N (N-Q, 401.2 eV), and pyridinic-N⁺-O⁻ (N-O, 403.1 eV) [51]. Of these N functionalities, the content of N-6 groups is the highest, reaching 44.68 at% for NHCSF-0 and 47.13 at% for NHCSF-3 based on N 1s spectrum. It illustrates that pyridinic N is dominated in both samples under specific pyrolysis conditions. Here, N-5 and N-6 groups might induce the surface polarization of the carbon giving rise to the enhancement of the specific capacitance [8]. Also, higher N-Q content in NHCSF-3 might quicken the electron transfer [8,52−54]. For O 1s spectrum (Fig. 5c), the peaks around 531.0 eV, 532.1 eV, and 533.3 eV, are attributed to C=O (O-I), C−OH/C−O−C (O-II), and −COOH (O-III) species [55], respectively. Rich N and O functionalities (20.29 at% N and 8.27 at% O elements) on the NHCSF-3 surface would enhance the electrochemical activity of the electrode material and wettability of the electrolyte-electrode interface realizing high utilization of active material and the improvement of the capacitive performance [56]. For g-C₃N₄, the peaks corresponding to sp²-hybridized N in C-N=C (398.4 eV), tertiary nitrogen N-(C)₃ (399.6 eV) and N-H (400.9 eV) bonds are observed in the N 1s spectrum (Fig. S2b), which well matches with

**Table 2**
Chemical composition obtained from XPS analysis for NHCSF-0 and NHCSF-3.

| Sample	Element composition/at %			N 1s/%			
	C	N	O	N-6	N-5	N-Q	N-O
NHCSF-0	73.44	20.04	6.52	44.68	38.59	11.23	5.5
NHCSF-3	71.44	20.29	8.27	47.13	25.81	23.89	3.17

the result reported [57]. Also, the C−OH/C−O−C (O-II) bond appears at 532.1 eV in the O 1s spectrum of g-C₃N₄ (Fig. S2c). The above results infer that both NHCSF-0 and NHCSF-3 are significant from g-C₃N₄ in surface chemistry.

In order to further understand high-N structure of NHCSF-3, FTIR spectra of g-C₃N₄ and NHCSF-3 are depicted in Fig. S3. Characteristic bands of g-C₃N₄, such as the breathing vibration of triazine units at 806 cm⁻¹, the skeletal vibrations of N-containing groups at 1245-1640 cm⁻¹, and the stretching of −OH/-NH groups at 3213 cm⁻¹, are observed [57,58]. For the NHCSF-3, no peak reflecting triazine units appears, and the peaks at 1281, 1600, and 3417 cm⁻¹ are attributed to N-H, C=N, and −OH/-NH groups [59], respectively. Additionally, a weak band at 2215 cm⁻¹ may be attributed to the nitrile C≡N group [59]. With respect to this, Chen et al. pointed out that not all N atoms are incorporated into the graphitic lattice because a high N-doped content can result in structural instability, and some N atoms exist as C≡N species in the resulting N-doped carbon [59]. From XRD, XPS and FTIR results, it is confirmed that g-C₃N₄ and NHCSF-3 have different structures, and NHCSF-3 may be a N-rich carbon material with small amount of C≡N species absorbed in porous NHCSF-3.
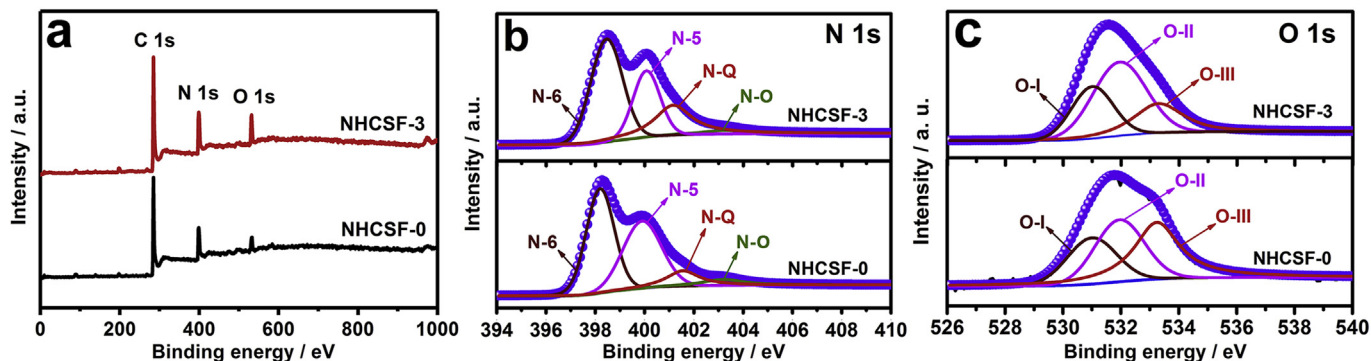
Fig. 5. (a) XPS survey spectra of NHCSF-0 and NHCSF-3; high-resolution (b) N 1s and (c) O 1s XPS spectra of NHCSF-0 and NHCSF-3. (A colour version of this figure can be viewed online.)
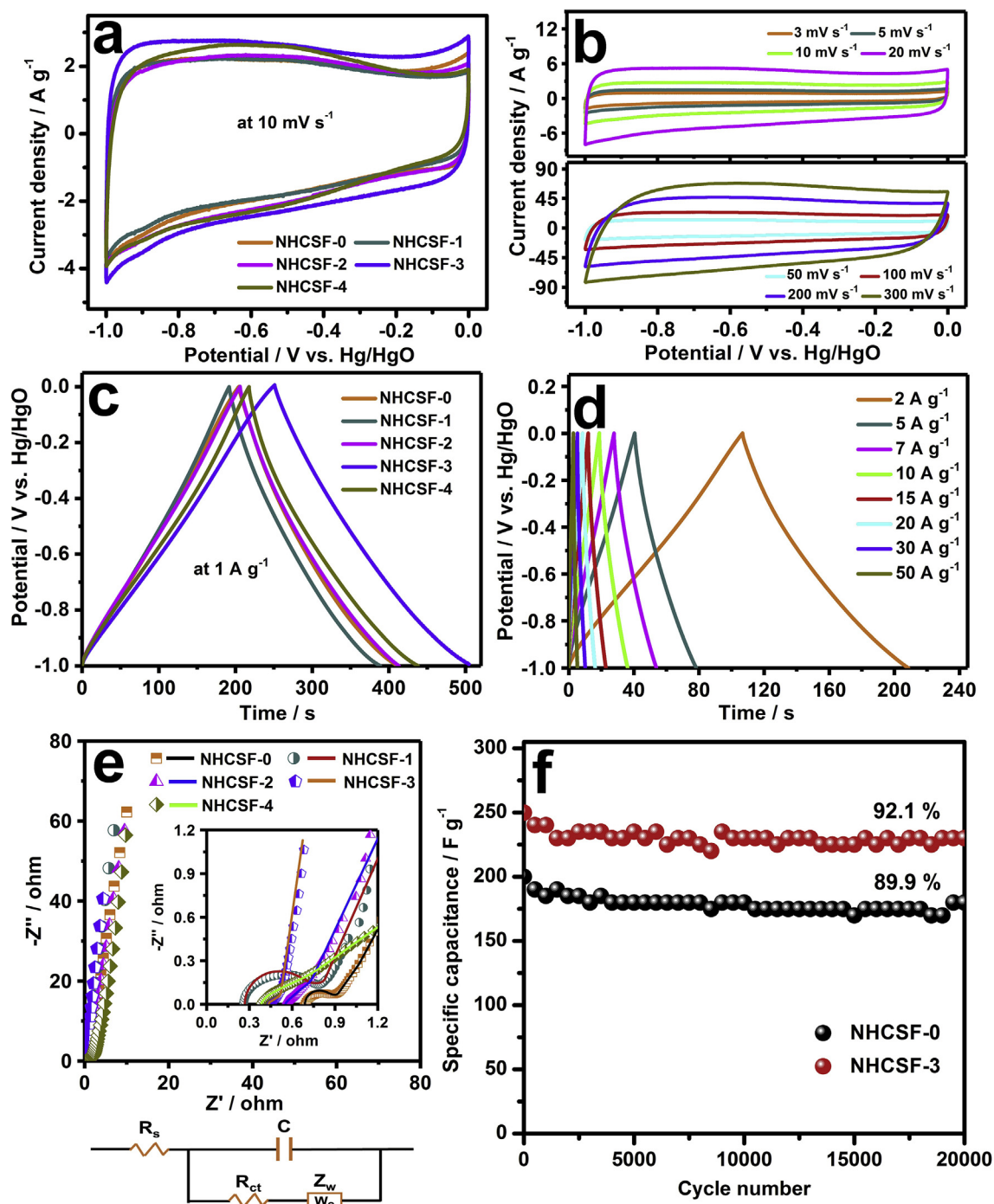
Fig. 6. (a) CV profiles of NHCSFs at a scan rate of 10 mV s^{-1}; (b) CV profiles of NHCSF-3 at various scan rates (3−300 mV s^{-1}); (c) GCD profiles of NHCSFs at a current density of 1 A g^{-1}; (d) GCD profiles of NHCSF-3 at various current densities (2−50 A g^{-1}); (e) Nyquist plots and equivalent circuit of NHCSFs (the inset showing the magnified plots); (f) cycling stability of NHCSF-0 and NHCSF-3 at a current density of 4 A g^{-1}. (A colour version of this figure can be viewed online.)

3.5. Electrochemical behavior in a three-electrode setup in alkaline electrolyte

Supercapacitive properties of NHCSFs are examined by cyclic voltammetry (CV), galvanostatic charge-discharge (GCD), and electrochemical impedance spectroscopy (EIS) tests in a 6 M KOH aqueous electrolyte. In Fig. 6a, all CV curves show quasi-rectangular profiles with weak redox peaks, which indicate that NHCSFs have a typical EDLC behavior and deliver additional pesoducapacitance

mainly arising from N and O species undergoing redox reactions. Bigger integral area for NHCSF-3 than for other four samples may be an indication of higher capacitance in NHCSF-3. In Fig. 6b, as the scan rate increases from 3 to 300 mV s^{-1}, the current response is promoted with a slight shape change, verifying nearly ideal capacitive nature and good rate profile of NHCSF-3. The possible redox reactions from N and O species are described as follows [51,60]:

$$\text{(pyridine)N-H} + 2OH^- \longleftrightarrow \text{(pyridine)N-OH} + H_2O + 2e^- \tag{1}$$

$$\text{(pyrrole):NH} + OH^- \longleftrightarrow \text{(pyrrole}^{\ominus}):NH + H_2O + e^- \tag{2}$$

$$>COOH + OH^- \longleftrightarrow >COO^- + H_2O + e^- \tag{3}$$

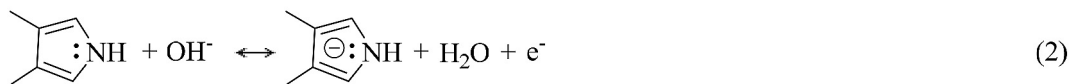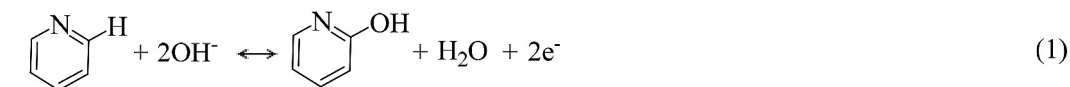$$>C\text{-}OH + OH^- \longleftrightarrow >C=O + H_2O + e^- \tag{4}$$

Fig. 6c and d presents GCD profiles for gaining capacitance values and evaluating the rate behavior of NHCSF-3. Among various NHCSFs, the NHCSF-3 has the longest discharge time (Fig. 6c). Moreover, its GCD curves at a wide rate range of $2-50\,A\,g^{-1}$ are approximately symmetrical (Fig. 6d), which is companied with CV results to well prove the electrochemical reversibility of NHCSF-3 as EDLC electrode. On the basis of discharge curves in Fig. 6c, the order of C_m value is NHCSF-3 $(253.6\,F\,g^{-1})$ > NHCSF-4 $(219.5\,F\,g^{-1})$ > NHCSF-0 $(208.4\,F\,g^{-1})$ > NHCSF-2 $(208.2\,F\,g^{-1})$ > NHCSF-1 $(198.5\,F\,g^{-1})$. In spite of slightly low BET area for NHCSF-3, it delivers higher C_m value than NHCSF-0. Recent studies from other groups also reported similar finding that low-area carbon materials deliver high specific capacitances [5,55,61–65]. This indicates that the capacitance not only depends on the BET area but also on other pore properties (e.g., the size and morphology of pores, hierarchical porosity, and pore volume). Attractively, a high value of $200.4\,F\,g^{-1}$ is retained even when discharged at a fast $50\,A\,g^{-1}$ rate (Fig. 6d), verifying fast ion diffusion and high-rate charge storage profile [66]. Further, electrochemical results of all carbons are summarized in Table 3. It is seen that C_m values of all samples reduce gradually with the increase of current density, which might be attributed to inadequate time for ion diffusion into the pores, as verified in literature [5,67]. By contrast, NHCSF-3 has the best electrochemical properties.

In addition, electrochemical properties of g-C_3N_4 are presented in Fig. S4. Fig. S4a shows the CV curve of g-C_3N_4 at a scan rate of $10\,mV\,s^{-1}$. Compared with NHCSF-3, g-C_3N_4 has not the characteristic of EDLC behavior, and its enclosed CV area is negligible indicating no capacitance on g-C_3N_4. The GCD curve in Fig. S4b reveals that the capacitance of g-C_3N_4 is quite low (about $1.1\,F\,g^{-1}$ at $1\,A\,g^{-1}$). Thus, both samples have different electrochemical behaviors, and the latter is a typical EDLC material.

Electrochemical activity of NHCSFs is evaluated with Nyquist plots (Fig. 6e). Also, equivalent circuit is displayed in Fig. 6e, and the related parameters are listed in Table 3. Similar impedance features can be seen in all samples. However, NHCSF-3 exhibits the most vertical line at low frequency, indicating nearly ideal capacitive behavior and high pore accessibility for ions. Its high-frequency

semicircle corresponding to R_{ct} (charge-transfer resistance, $0.02\,\Omega$) is the smallest (inset in Fig. 6e), revealing fast electron transfer. Meanwhile, NHCSF-3 possesses the smallest Z_w (Warburg resistance, $0.21\,\Omega$) reflecting smooth transport of the ions inside the pores. From the inset in Fig. 6e, the R_s (internal resistance) value of NHCSF-3 is evaluated to $0.44\,\Omega$ in very high frequency, which is nearly the lowest value. Consequently, NHCSF-3 shows high electrochemical activity. The stability of NHCSF-0 and NHCSF-3 is examined by successive galvanostatic tests at $4\,A\,g^{-1}$ current density. As shown in Fig. 6f, NHCSF-3 can retain 92.1% of initial capacitance (a low decay rate of ~0.04% per cycle) up to 20000 cycles, higher than the value of NHCSF-0 (89.9%), demonstrating excellent electrochemical durability for NHCSF-3.

3.6. Electrochemical behavior in a two-electrode setup in alkaline and neutral electrolytes

Table S1 provides a performance comparison of NHCSF-3 with carbon materials reported in literatures. Obviously, NHCSF-3 possesses a competitive performance in term of specific capacitance, rate capability, and cycling performance. As such, the NHCSF-3 based alkaline and neutral SCs in a symmetrical mode are assembled and evaluated as follows. In an alkaline device, rectangular CV (Fig. S5a) and triangular GCD curves (Fig. S5b) with high symmetry even at fairly high scan rate and current density prove ideal electrochemical capacitive properties with high rate capability $(135.4\,F\,g^{-1}$ for single electrode at $30\,A\,g^{-1}$, 76% retention), responsible for high power performance (Fig. S5c).

The details of the performance in neutral SCs are presented in Fig. 7. The investigation on the potential window reveals that the window of 1.6 V for neutral SCs is feasible since too high window up to 1.8 V arises from a relatively fast increase of anodic current density possibly inferring the decomposition of the electrolyte (Fig. 7a). Low OH^- concentration should contribute to the enlarged window in Na_2SO_4 electrolyte. Based on GCD curves at current density ranging from $1\,A\,g^{-1}$ to $10\,A\,g^{-1}$ (Fig. 7b), C_s values are $150\,F\,g^{-1}$, $142.9\,F\,g^{-1}$, $119.9\,F\,g^{-1}$, $109.2\,F\,g^{-1}$, and $91.1\,F\,g^{-1}$, showing relatively high rate capability [5]. Energy and power densities in both electrolytes are calculated using eqns. (3) and (4), and plotted

**Table 3**
Parameters of equivalent circuit, C_m values at various current densities and rate retention of different NHCSFs.

Sampl'e	R_s/Ω	R_{ct}/Ω	Z_w/Ω	C_m at different current density/F g^{-1}						Rate retention/%
				1	5	10	20	30	50[a]	
NHCSF-0	0.69	0.17	0.22	208.4	185.1	176.0	166.8	156.9	142.6	68.4
NHCSF-1	0.27	0.42	0.5	198.5	177.6	172.7	164.1	160.6	151.7	76.4
NHCSF-2	0.55	0.06	0.55	208.2	189.4	179.6	167.0	163.9	162.1	77.9
NHCSF-3	0.44	0.02	0.21	253.6	228.5	219.5	210.2	207.9	200.4	79.0
NHCSF-4	0.38	0.17	4.37	219.5	200.0	190.2	170.8	166.4	145.2	66.2

[a] Current density from $1\,A\,g^{-1}$ to $50\,A\,g^{-1}$.
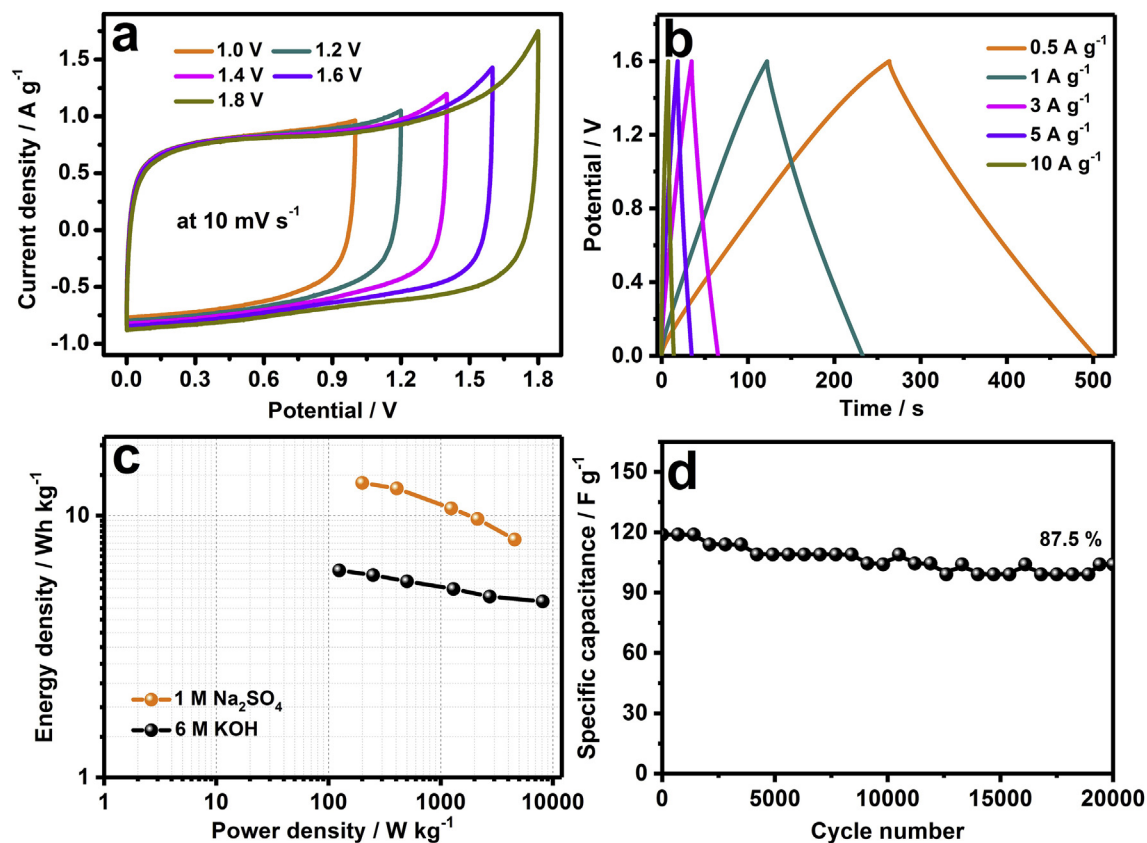
Fig. 7. NHCSF-3 based neutral SCs: (a) CV curves at various potential windows; (b) GCD curves at various current densities; (c) Ragone plots; (d) cycling stability at a current density of 4 A g^{-1} over 20000 cycles. (A colour version of this figure can be viewed online.)
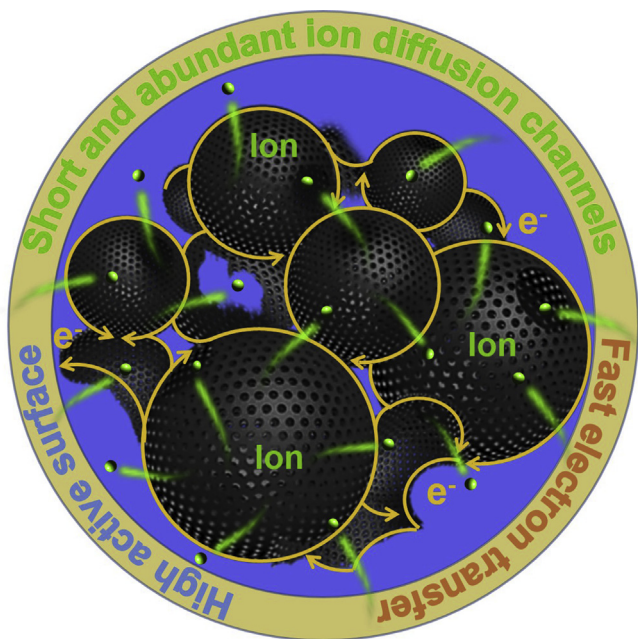
Fig. 8. Scheme illustrating effective electron and ion transfer within NHCSF-3. (A colour version of this figure can be viewed online.)

in Fig. 7c for comparison. Apparently, neutral SCs exhibit the dramatically increased energy density (13.33 Wh kg^{-1}) compared with alkaline SCs (6.17 Wh kg^{-1}). The promoted energy density should be attributed to the enlarged voltage window in a neutral electrolyte. Fig. 7d accounts for outstanding stability of neutral SCs, with 87.5% capacitance retention over 20000 cycles.

Ideally capacitive charge storage profile should be profited mainly from unique tailor-formed framework structures and high N-doping level in the following aspects (Fig. 8). Hollow reservoir-like structures with porous walls, high BET area and hierarchical open porosity not only quicken the electrolyte ion mobility especially at high rates but also preserve more electrolyte in voids, enabling highly efficient ion transportation in NHCSF-3 [5,68]; Thin and hollow structure shortens the ion diffusion paths; 3D frameworks of integrating hollow shells and nanoflakes create electronically connecting networks fastening the charge transfer, and promote electrochemical stability of the materials; High heteroatom (N, O) content endows the carbon surface with rich active sites for charge storage. Consequently, the promise of the as-fabricated NHCSF-3 as a functional material in SCs and/or other renewable energy applications may be expected.

4. Conclusions

In summary, we report our findings in the design and fabrication of a unique form of hollow carbon frameworks using the engineered core-shell ZIF-8/PP-SiO₂ precursors by the simple layer-by-layer assembly and subsequent pyrolysis in N₂ flow. The morphology and pore structure of formed carbons can be well controlled by tuning the amount of added SiO₂, yielding the optimized architectures with multiple advantages of hollow porous shells and thin porous nanoflakes, such as short and abundant ion diffusion channels, fast electron transfer, high active surface as well as efficient electrolyte reservoirs and high accommodation ability

for volume expansion. Therefore, NHCSF-3 achieves high specific capacitance of 253.6 F g^{-1} at 1 A g^{-1}, excellent rate capability up to 50 A g^{-1}, and outstanding stability with a retention of 92.1% for 20000 cycles. Furthermore, neutral SCs show high priority in energy density (13.33 Wh kg^{-1}), which make NHCSF-3 hold great importance for energy applications.

Conflicts of interest

The authors declare no competing financial interest.

Acknowledgements

Appendix A. Supplementary data

Supplementary data related to this article can be found at https://doi.org/10.1016/j.carbon.2018.04.075.

References

[1] M.F. El-Kady, V. Strong, S. Dubin, R.B. Kaner, Laser scribing of high-performance and flexible graphene-based electrochemical capacitors, Science 335 (6074) (2012) 1326–1330.

[2] J.R. Miller, P. Simon, Materials science: electrochemical capacitors for energy management, Science 321 (5889) (2008) 651–652.

[3] Y. Zhu, S. Murali, M.D. Stoller, K.J. Ganesh, W. Cai, P.J. Ferreira, et al., Carbon-based supercapacitors produced by activation of graphene, Science 332 (6037) (2011) 1537–1541.

[4] Z.S. Wu, K. Parvez, X. Feng, K. Müllen, Graphene-based in-plane micro-supercapacitors with high power and energy densities, Nat. Commun. (2013) 4.

[5] C. Long, X. Chen, L. Jiang, L. Zhi, Z. Fan, Porous layer-stacking carbon derived from in-built template in biomass for high volumetric performance supercapacitors, Nanomater. Energy 12 (2015) 141–151.

[6] L. Liu, Z. Niu, J. Chen, Unconventional supercapacitors from nanocarbon-based electrode materials to device configurations, Chem. Soc. Rev. 45 (15) (2016) 4340–4363.

[7] Q. Wang, J. Yan, Z. Fan, Carbon materials for high volumetric performance supercapacitors: design, progress, challenges and opportunities, Energy Environ. Sci. 9 (3) (2016) 729–762.

[8] F. Sun, H. Wu, X. Liu, F. Liu, H. Zhou, J. Gao, et al., Nitrogen-rich carbon spheres made by a continuous spraying process for high-performance supercapacitors, Nano Res. 9 (11) (2016) 3209–3221.

[9] A. Sanchez-Sanchez, M.T. Izquierdo, S. Mathieu, J. González-Álvarez, A. Celzard, V. Fierro, Outstanding electrochemical performance of highly N- and O-doped carbons derived from pine tannin, Green Chem. 19 (11) (2017) 2653–2665.

[10] F. Xu, Z. Tang, S. Huang, L. Chen, Y. Liang, W. Mai, et al., Facile synthesis of ultrahigh-surface-area hollow carbon nanospheres for enhanced adsorption and energy storage, Nat. Commun. 6 (2015) 7221.

[11] X. Lai, J.E. Halpert, D. Wang, Recent advances in micro-/nano-structured hollow spheres for energy applications: from simple to complex systems, Energy Environ. Sci. 5 (2) (2012) 5604–5618.

[12] L.-F. Chen, Y. Lu, L. Yu, X.W. Lou, Designed formation of hollow particle-based nitrogen-doped carbon nanofibers for high-performance supercapacitors, Energy Environ. Sci. 10 (8) (2017) 1777–1783.

[13] R.J. White, K. Tauer, M. Antonietti, M.M. Titirici, Functional hollow carbon nanospheres by latex templating, J. Am. Chem. Soc. 132 (49) (2010) 17360–17363.

[14] S. Li, A. Pasc, V. Fierro, A. Celzard, Hollow carbon spheres, synthesis and applications – a review, J. Mater. Chem. 4 (33) (2016) 12686–12713.

[15] F. Böttger-Hiller, P. Kempe, G. Cox, A. Panchenko, N. Janssen, A. Petzold, et al., Twin polymerization at spherical hard templates: an approach to size-

[16] adjustable carbon hollow spheres with micro- or mesoporous shells, Angew. Chem. Int. Ed. 52 (23) (2013) 6088–6091.

[16] Z.A. Qiao, B. Guo, A.J. Binder, J. Chen, G.M. Veith, S. Dai, Controlled synthesis of mesoporous carbon nanostructures via a "Silica-assisted" strategy, Nano Lett. 13 (1) (2013) 207–212.

[17] X. Chen, K. Kierzek, K. Cendrowski, I. Pelech, X. Zhao, J. Feng, et al., CVD generated mesoporous hollow carbon spheres as supercapacitors, Colloid. Surface. 396 (2012) 246–250.

[18] Y. Han, X. Dong, C. Zhang, S. Liu, Hierarchical porous carbon hollow-spheres as a high performance electrical double-layer capacitor material, J. Power Sources 211 (2012) 92–96.

[19] S. Mezzavilla, C. Baldizzone, K.J.J. Mayrhofer, F. Schüth, General method for the synthesis of hollow mesoporous carbon spheres with tunable textural properties, ACS Appl. Mater. Interfaces 7 (23) (2015) 12914–12922.

[20] X. Liu, N. Wen, X. Wang, Y. Zheng, A high-performance hierarchical graphene@polyaniline@graphene sandwich containing hollow structures for supercapacitor electrodes, ACS Sustain. Chem. Eng. 3 (3) (2015) 475–482.

[21] M. Pérez-Page, E. Yu, J. Li, M. Rahman, D.M. Dryden, R. Vidu, et al., Template-based syntheses for shape controlled nanostructures, Adv. Colloid Interface 234 (2016) 51–79.

[22] F. Ran, X. Zhang, Y. Liu, K. Shen, X. Niu, Y. Tan, et al., Super long-life supercapacitor electrode materials based on hierarchical porous hollow carbon microcapsules, RSC Adv. 5 (106) (2015) 87077–87083.

[23] W.-W. Zhan, Q. Kuang, J.-Z. Zhou, X.-J. Kong, Z.-X. Xie, L.-S. Zheng, Semiconductor@metal—organic framework core—shell heterostructures: a case of ZnO@ZIF-8 nanorods with selective photoelectrochemical response, J. Am. Chem. Soc. 135 (5) (2013), 1926-33.

[24] J. Han, G. Xu, B. Ding, J. Pan, H. Dou, D.R. MacFarlane, Porous nitrogen-doped hollow carbon spheres derived from polyaniline for high performance supercapacitors, J. Mater. Chem. 2 (15) (2014) 5352–5357.

[25] L. Liu, S.-D. Xu, Q. Yu, F.-Y. Wang, H.-L. Zhu, R.-L. Zhang, et al., Nitrogen-doped hollow carbon spheres with a wrinkled surface: their one-pot carbonization synthesis and supercapacitor properties, Chem. Commun. 52 (78) (2016) 11693–11696.

[26] X. Liu, L. Zhou, Y. Zhao, L. Bian, X. Feng, Q. Pu, Hollow, spherical nitrogen-rich porous carbon shells obtained from a porous organic framework for the supercapacitor, ACS Appl. Mater. Interfaces 5 (20) (2013) 10280–10287.

[27] C. Liu, J. Wang, J. Li, M. Zeng, R. Luo, J. Shen, et al., Synthesis of N-Doped hollow-structured mesoporous carbon nanospheres for high-performance supercapacitors, ACS Appl. Mater. Interfaces 8 (11) (2016) 7194–7204.

[28] L. Wang, G. Zhang, X. Zhang, H. Shi, W. Zeng, H. Zhang, et al., Porous ultrathin carbon nanobubbles formed carbon nanofiber webs for high-performance flexible supercapacitors, J. Mater. Chem. 5 (28) (2017) 14801–14810.

[29] E. Frackowiak, Carbon materials for supercapacitor application, Phys. Chem. Chem. Phys. 9 (15) (2007) 1774.

[30] K. Gopalsamy, J. Balamurugan, T.D. Thanh, N.H. Kim, J.H. Lee, Fabrication of nitrogen and sulfur co-doped graphene nanoribbons with porous architecture for high-performance supercapacitors, Chem. Eng. J. 312 (2017) 180–190.

[31] Y. Pan, M. Xue, M. Chen, Q. Fang, L. Zhu, V. Valtchev, et al., ZIF-derived in situ nitrogen decorated porous carbons for CO$_2$ capture, Inorg. Chem. Front. 3 (9) (2016) 1112–1118.

[32] B. Liu, H. Shioyama, T. Akita, Q. Xu, Metal-organic framework as a template for porous carbon synthesis, J. Am. Chem. Soc. 130 (16) (2008) 5390–5391.

[33] J. Tang, Y. Yamauchi, Carbon materials: MOF morphologies in control, Nat. Chem. 8 (7) (2016) 638–639.

[34] H. Zhang, J. Nai, L. Yu, X.W. Lou, Metal-organic-framework-based materials as platforms for renewable energy and environmental applications, Joule 1 (1) (2017) 77–107.

[35] Y.V. Kaneti, J. Tang, R.R. Salunkhe, X. Jiang, A. Yu, K.C.W. Wu, et al., Nano-architectured design of porous materials and nanocomposites from metal-organic frameworks, Adv. Mater. 29 (12) (2017), 1604898.

[36] W. Zhang, X. Jiang, Y. Zhao, A. Carné-Sánchez, V. Malgras, J. Kim, et al., Hollow carbon nanobubbles: monocrystalline MOF nanobubbles and their pyrolysis, Chem. Sci. 8 (5) (2017) 3538–3546.

[37] W. Chaikittisilp, M. Hu, H. Wang, H.-S. Huang, T. Fujita, K.C.W. Wu, et al., Nanoporous carbons through direct carbonization of a zeolitic imidazolate framework for supercapacitor electrodes, Chem. Commun. 48 (58) (2012) 7259.

[38] M. Shaibani, S.J.D. Smith, P.C. Banerjee, K. Konstas, A. Zafari, D.E. Lobo, et al., Framework-mediated synthesis of highly microporous onion-like carbon: energy enhancement in supercapacitors without compromising power, J. Mater. Chem. 5 (6) (2017) 2519–2529.

[39] M. Klose, R. Reinhold, K. Pinkert, M. Uhlemann, F. Wolke, J. Balach, et al., Hierarchically nanostructured hollow carbon nanospheres for ultrafast and long-life energy storage, Carbon 106 (2016) 306–313.

[40] W. Bao, A.K. Mondal, J. Xu, C. Wang, D. Su, G. Wang, 3D hybrid–porous carbon derived from carbonization of metal organic frameworks for high performance supercapacitors, J. Power Sources 325 (2016) 286–291.

[41] C. Young, R.R. Salunkhe, J. Tang, C.-C. Hu, M. Shahabuddin, E. Yanmaz, et al., Zeolitic imidazolate framework (ZIF-8) derived nanoporous carbon: the effect of carbonization temperature on the supercapacitor performance in an aqueous electrolyte, Phys. Chem. Chem. Phys. 18 (42) (2016) 29308–29315.

[42] Y. Wang, B. Chen, Y. Zhang, L. Fu, Y. Zhu, L. Zhang, et al., ZIF-8@MWCNT-derived carbon composite as electrode of high performance for supercapacitor, Electrochim. Acta 213 (2016) 260–269.

[43] Y.-Y. Fu, C.-X. Yang, X.-P. Yan, Fabrication of ZIF-8@SiO2 core—shell micro-spheres as the stationary phase for high-performance liquid chromatography, Chem. Eur J. 19 (40) (2013) 13484—13491.

[44] D.J. Martin, K. Qiu, S.A. Shevlin, A.D. Handoko, X. Chen, Z. Guo, et al., Highly efficient photocatalytic H_2 evolution from water using visible light and structure-controlled graphitic carbon nitride, Angew. Chem. Int. Ed. 53 (35) (2014) 9240—9245.

[45] A. Schejn, L. Balan, V. Falk, L. Aranda, G. Medjahdi, R. Schneider, Controlling ZIF-8 nano- and microcrystal formation and reactivity through zinc salt var-iations, CrystEngComm 16 (21) (2014) 4493—4500.

[46] Y. Pan, Y. Liu, G. Zeng, L. Zhao, Z. Lai, Rapid synthesis of zeolitic imidazolate framework-8 (ZIF-8) nanocrystals in an aqueous system, Chem. Commun. 47 (7) (2011) 2071.

[47] H. Kobayashi, Y. Mitsuka, H. Kitagawa, Metal nanoparticles covered with a metal—organic framework: from one-pot synthetic methods to synergistic energy storage and conversion functions, Inorg. Chem. 55 (15) (2016) 7301—7310.

[48] F. Bai, Y. Xia, B. Chen, H. Su, Y. Zhu, Preparation and carbon dioxide uptake capacity of N-doped porous carbon materials derived from direct carboniza-tion of zeolitic imidazolate framework, Carbon 79 (2014) 213—226.

[49] W. Lei, W. Xiao, J. Li, G. Li, Z. Wu, C. Xuan, et al., Highly nitrogen-doped three-dimensional carbon fibers network with superior sodium storage capacity, ACS Appl. Mater. Interfaces 9 (34) (2017) 28604—28611.

[50] Y. Xie, Y. Chen, L. Liu, P. Tao, M. Fan, N. Xu, et al., Ultra-high pyridinic N-doped porous carbon monolith enabling high-capacity K-ion battery anodes for both half-cell and full-cell applications, Adv. Mater. 29 (35) (2017), 1702268.

[51] C. Tang, Y. Liu, D. Yang, M. Yang, H. Li, Oxygen and nitrogen co-doped porous carbons with finely-layered schistose structure for high-rate-performance supercapacitors, Carbon 122 (2017) 538—546.

[52] C.O. Ania, V. Khomenko, E. Raymundo-Piñero, J.B. Parra, F. Béguin, The large electrochemical capacitance of microporous doped carbon obtained by using a zeolite template, Adv. Funct. Mater. 17 (11) (2007) 1828—1836.

[53] J. Wu, D. Zhang, Y. Wang, B. Hou, Electrocatalytic activity of nitrogen-doped graphene synthesized via a one-pot hydrothermal process towards oxygen reduction reaction, J. Power Sources 227 (2013) 185—190.

[54] W. Lu, M. Liu, L. Miao, D. Zhu, X. Wang, H. Duan, et al., Nitrogen-containing ultramicroporous carbon nanospheres for high performance supercapacitor electrodes, Electrochim. Acta 205 (2016) 132—141.

[55] J. Pang, W. Zhang, J. Zhang, G. Cao, M. Han, Y. Yang, Facile and sustainable synthesis of sodium lignosulfonate derived hierarchical porous carbons for supercapacitors with high volumetric energy densities, Green Chem. 19 (16) (2017) 3916—3926.

[56] D.-W. Wang, F. Li, L.-C. Yin, X. Lu, Z.-G. Chen, I.R. Gentle, et al., Nitrogen-doped carbon monolith for alkaline supercapacitors and understanding nitrogen-induced redox transitions, Chem. Eur J. 18 (17) (2012) 5345—5351.

[57] Y. Zeng, X. Liu, C. Liu, L. Wang, Y. Xia, S. Zhang, et al., Scalable one-step pro-duction of porous oxygen-doped g-C3N4 nanorods with effective electron separation for excellent visible-light photocatalytic activity, Appl. Catal. B Environ. 224 (2018) 1—9.

[58] J. Di, J. Xia, X. Li, M. Ji, H. Xu, Z. Chen, et al., Constructing confined surface carbon defects in ultrathin graphitic carbon nitride for photocatalytic free radical manipulation, Carbon 107 (2016) 1—10.

[59] F. Zheng, Y. Yang, Q. Chen, High lithium anodic performance of highly nitrogen-doped porous carbon prepared from a metal-organic framework, Nat. Commun. 5 (2014) 5261.

[60] J.-S. Wei, H. Ding, Y.-G. Wang, H.-M. Xiong, Hierarchical porous carbon ma-terials with high capacitance derived from Schiff-base networks, ACS Appl. Mater. Interfaces 7 (10) (2015) 5811—5819.

[61] X. Wu, W. Xing, J. Florek, J. Zhou, G. Wang, S. Zhuo, et al., On the origin of the high capacitance of carbon derived from seaweed with an apparently low surface area, J. Mater. Chem. 2 (44) (2014) 18998—19004.

[62] F. Zhang, T. Liu, M. Li, M. Yu, Y. Luo, Y. Tong, et al., Multiscale pore network boosts capacitance of carbon electrodes for ultrafast charging, Nano Lett. 17 (5) (2017) 3097—3104.

[63] Z. Li, Z. Xu, H. Wang, J. Ding, B. Zahiri, C.M.B. Holt, et al., Colossal pseudoca-pacitance in a high functionality—high surface area carbon anode doubles the energy of an asymmetric supercapacitor, Energy Environ. Sci. 7 (5) (2014) 1708—1718.

[64] P. Hao, Z. Zhao, J. Tian, H. Li, Y. Sang, G. Yu, et al., Hierarchical porous carbon aerogel derived from bagasse for high performance supercapacitor electrode, Nanoscale 6 (20) (2014) 12120—12129.

[65] P. Cheng, T. Li, H. Yu, L. Zhi, Z. Liu, Z. Lei, Biomass-derived carbon fiber aerogel as a binder-free electrode for high-rate supercapacitors, J. Phys. Chem. C 120 (4) (2016) 2079-86.

[66] J. Wang, J. Tang, B. Ding, V. Malgras, Z. Chang, X. Hao, et al., Hierarchical porous carbons with layer-by-layer motif architectures from confined soft-template self-assembly in layered materials, Nat. Commun. 8 (2017) 15717.

[67] C. Chen, D. Yu, G. Zhao, B. Du, W. Tang, L. Sun, et al., Three-dimensional scaffolding framework of porous carbon nanosheets derived from plant wastes for high-performance supercapacitors, Nanomater. Energy 27 (2016) 377—389.

[68] T. Liu, F. Zhang, Y. Song, Y. Li, Revitalizing carbon supercapacitor electrodes with hierarchical porous structures, J. Mater. Chem. 5 (34) (2017) 17705—17733.